Supporting Information

High-Performance Multiple-Resonance Thermally Activated Delayed Fluorescence Emitter with Targeted Deuteration Donor

Yixuan Jiang[a†], Yangze Xu[a†], Zihan Su[a], Xiaobo Ma[a], Futong Liu[a], Zhiming Wang[b], and Ping Lu[a*]*

[a] State Key Laboratory of Supramolecular Structure and Materials, College of Chemistry, Jilin University, Changchun 130012, P. R. China.

Corresponding Authors

Futong Liu, E-mail: liuft@jlu.edu.cn

Ping Lu, E-mail: lup@jlu.edu.cn

[b] State Key Laboratory of Luminescent Materials and Devices, Guangdong Provincial Key Laboratory of Luminescence from Molecular Aggregates, South China University of Technology, Guangzhou 510640, (P. R. China).

† These authors contributed equally.

Contents

1. Experimental section

1.1 General information

All the reagents and solvents were used as received without further purification. ^{1}H NMR, and ^{13}C NMR were recorded by Bruker AVANCE 500 spectrometer at 500 MHz or 125 MHz with tetramethylsilane (TMS) as the internal standard. Elemental analysis was carried out on a Flash EA 1112, CHNSO elemental analysis instrument. MALDI-TOF-MS mass spectra were obtained from an AXIMA-CFRTM plus instrument. BOF-5-50 vacuum sublimation instrument (AnHui BEQ Equipment Technology CO., Ltd) was used to sublimate the target compound. Thermal gravimetric analysis (TGA) was performed on a Perkin-Elmer thermal analysis system from 30 °C to 900 °C. Differential scanning calorimetry (DSC) was measured by NETZSCH (DSC-204) unit from 30 °C to 350 °C. Organic films for optical measurements were fabricated by thermal evaporation under high vacuum onto clean quartz substrates. UV-Vis absorption spectra were recorded on a Shimadzu UV-3100 spectrophotometer. Steady-state photoluminescence (PL) spectra were measured on an RF-5301PC spectrophotometer. Time-resolved photoluminescence measurements were performed on Edinburgh spectrometer LP980 365-nm laser flash as excitation source. The PL lifetime was measured using an FLS980 spectrometer with a 375-nm picosecond pulsed light-emitting diode excitation source (pulse width: 898.3 ps). The photoluminescence quantum yields (Φ_{PL}) were measured using an integrating sphere.

1.2 Electrochemical measurements

Cyclic voltammetry (CV) was measured using a BAS 100B/W electrochemical analyzer with a standard one-compartment, three-electrode electrochemical cell. Tetrabutylammoniumhexafluorophosphate ($TBAPF_6$) in anhydrous DCM (0.1 M) was used as the electrolyte for positive scans. The working electrode was a glass-carbon

disk electrode. The counter electrode was a Pt wire. The reference electrode was Ag/Ag^+. A ferrocenium/ferrocene (Fc^+/Fc) redox couple was used as the internal standard, and the formal potential of Fc^+/Fc is 4.8 eV below vacuum. All potentials relative to Ag/Ag^+ electrode obtained from CV measurement were referenced against Fc^+/Fc to calculate HOMO levels. As a result, the Ag/Ag^+ electrode is just a pseudo-reference. The HOMO/LUMO levels are calculated according to the following formalism:

$$E_{HOMO} = - (E_{ox} \text{ vs. } Fc^+/Fc + 4.8) \text{ eV} \quad \text{(S1)}$$

$$E_{LUMO} = E_{HOMO} + E_g \quad \text{(S2)}$$

where the E_{ox} vs. Fc^+/Fc is oxidation onset potentials relative to Fc^+/Fc reference, and E_g is obtained from the absorption edges of normalized absorption spectra in dilute toluene solution (10^{-5} M) at room temperature.

1.3 Device fabrications and measurements

The bottom emission device structure of the MR-TADF OLED used was indium tin oxide (ITO)/HATCN (5 nm)/TAPC (30 nm)/TCTA (5 nm)/mCP (5 nm)/x wt% emitters in PhCzBCz (20 nm)/TmPyPb (40 nm)/LiF (1 nm)/Al (120 nm), where ITO, HATCN (1,4,5,8,9,11- hexaazatriphenylene-hexacarbonitrile), TAPC (di-[4-(*N*,*N*-ditolyl-amino)-phenyl] cyclohexane), TCTA (4,4',4"-tri(*N*-carbazolyl)-triphenylamine), mCP (N,N'-dicarbazolyl-3,5-benzene), TmPyPb (3,3′-[5′-[3-(3-Pyridinyl) phenyl][1,1′:3′,1″-terphenyl]-3,3″-diyl]bispyridine), LiF (lithium fluoride) and Al were employed as the anode, hole injecting layer, hole transporting layer, buffer layer, exciton blocking layer, electron transporting layer, electron injecting layer and cathode, respectively. PhCzBCz (9-(2-(9-phenyl-9*H*-carbazol-3-yl)phenyl)-9*H*-3,9'-bicarbazole) was chosen as the host for the MR-TADF emitters. mCBP 3,3′-di(9H-carbazol-9-yl)-1,1′-biphenyl and 2,6-DCzPPy 2,6-bis(3-(carbazol-9-yl) phenyl)pyridine were also chosen as the host for the MR-TADF emitters. ITO coated glasses with a sheet resistance of 20 Ω $square^{-1}$ were used as the substrate and cleaned by deionized water, isopropyl alcohol,

acetone and toluene. Then the ITO glasses were irradiated in UV-zone for 30 min. The deposition system for organic and metal deposition has a base pressure lower than 5×10^{-6} mbar. The hole injecting layer HATCN was deposited at 0.1 Å s^{-1}. The deposition rate of all other organic layers was 1.0 Å s^{-1}. The electron injecting layer LiF was deposited at a rate of 0.1 Å s^{-1} and then the capping Al metal layer was deposited at a rate of 4.0 Å s^{-1}. The electroluminescent (EL) characteristics were measured using a Keithley 2400 programmable electrometer and a PR-650 Spectroscan spectrometer under ambient condition at room temperature. The device operational lifetimes (LT_{50}) were evaluated by measuring the luminance over time at a constant current densities starting from an initial luminance of 1000 cd m^{-2}.

1.4 Theoretical calculations

The calculations were performed using the Density Functional Theory (DFT) implemented within Gaussian 16. We optimized the ground state using the B3LYP[3,4] and M06-2X functional with the 6-31G(d,p) basis set. The excited-state calculations were performed at Time-dependent DFT (TD-DFT) using the same functional and basis set as for ground-state geometry optimization to obtain the frontier molecular orbital (FMO) distribution, oscillator strength (*f*) values, vertical transitions and natural transition orbitals (NTOs) of the singlet and triplet states. PySOC was used for the calculation of the spin-orbit coupling matrix element (SOCME) values based on the optimized T_1 geometries.

1.5 Calculation Formulas for the Photophysical Parameters

The rate constants for radiative decay (k_r) and nonradiative decay (k_{nr}) from S_1 to S_0 states, the rate constants of intersystem crossing (k_{ISC}) and reverse intersystem crossing (k_{RISC}) were calculated from the following six equations:

$$k_p = 1/\tau_p \quad \text{(S5)}$$

$$k_d = 1/\tau_d \quad \text{(S6)}$$

$$k_r = \Phi_p k_p + \Phi_d k_d \approx \Phi_p k_p \quad \text{(S7)}$$

$$k_{nr} = (1 - \Phi_{PL})\, k_r / \Phi_{PL} \quad \text{(S8)}$$

$$k_{ISC} = k_p - k_r - k_{nr} \quad \text{(S9)}$$

$$k_{RISC} = k_p\, k_d\, \Phi_d / (k_{ISC}\, \Phi_p) \quad \text{(S10)}$$

Where τ_p and τ_d represent the prompt and decay fluorescence lifetime, which determined from transient PL spectra. The k_p and k_d represent the decay rate constants for prompt and delayed fluorescence, respectively. Φ_p and Φ_d indicate prompt and delayed fluorescence components and can be distinguished from the total Φ_{PL} by comparing the integrated intensities of prompt and delayed components in the transient PL spectra.

1.6 Synthetic procedures

All the reagents and solvents used for the syntheses were purchased from Aldrich and Acros and used as received. The precursor **DtCzB-Bpin** and **p-BrCzPhD** was prepared according to the procedure in literature.[1,2]

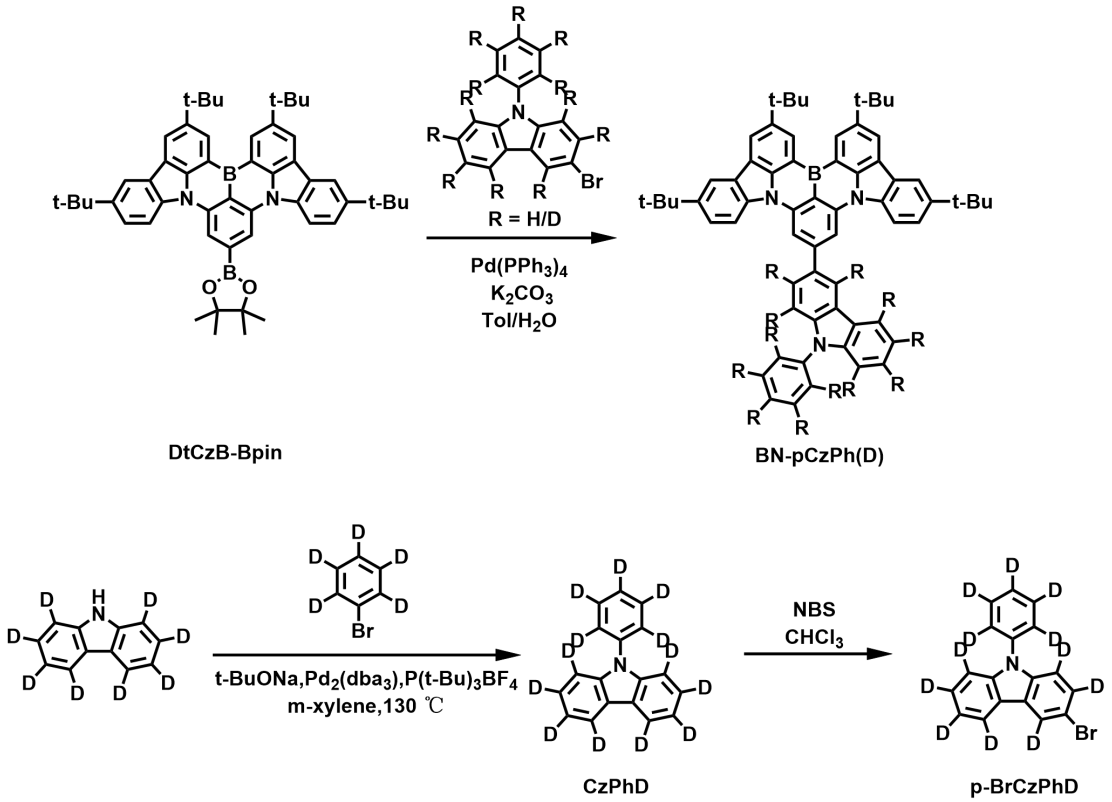

Scheme S1. Synthetic procedures of **BN-pCzPh** and **BN-pCzPhD**

Synthesis of BN-pCzPh: In a 100 mL round flask, a mixture of **DtCzB-Bpin** (766 mg, 1 mmol), 3-Bromo-9-phenyl-9H-carbazole (483 mg, 1.5 mmol), K_2CO_3 (5.52 g, 40 mmol), $Pd(PPh_3)_4$ (230 mg, 0.2 mmol), 20 mL distilled water and 40 mL toluene was heated to reflux and stirred under N_2 for 24 hours. The mixture was washed thrice with 30 mL water and extracted with DCM. The organic phase was collected and dried with anhydrous Na_2SO_4, and the slvent was evaporated. The residue was purified via column chromatography eluting with petroleum ether-DCM (4:1, v/v) mixtures to afford a yellow solid. (590 mg, **Yield:** 67%). **^{1}H NMR (500 MHz, $CDCl_3$) δ (ppm):** δ 9.17 (d, *J* = 1.9 Hz, 2H), 8.68 (d, *J* = 7.2 Hz, 3H), 8.56 – 8.47 (m, 4H), 8.35 (d, *J* = 7.7 Hz, 1H), 8.30 (d, *J* = 2.1 Hz, 2H), 8.04 (dd, *J* = 8.5, 1.9 Hz, 1H), 7.72 – 7.65 (m, 7H), 7.52 (dd, *J* = 23.5, 4.1 Hz, 3H), 7.39 (dt, *J* = 7.9, 4.2 Hz, 1H), 1.69 (s, 18H), 1.54 (s, 18H); **MALDI-TOF-MS:** $C_{64}H_{60}BN_3$ **Calculated:** 882.015; **Found:** 882.036.

Synthesis of BN-pCzPhD: In a 100 mL round flask, a mixture of **DtCzB-Bpin** (766 mg, 1 mmol), **p-BrCzPhD** (500 mg, 1.5 mmol), K_2CO_3 (5.52 g, 40 mmol), $Pd(PPh_3)_4$

(230 mg, 0.2 mmol), 20 mL distilled water and 40 mL toluene was heated to reflux and stirred under N_2 for 24 hours. The mixture was washed thrice with 30 mL water and extracted with DCM. The organic phase was collected and dried with anhydrous Na_2SO_4, and the solvent was evaporated. The residue was purified via column chromatography eluting with petroleum ether-DCM (4:1, v/v) mixtures to afford a yellow solid. (563 mg, **Yield:** 63%). **^{1}H NMR (500 MHz, $CDCl_3$) δ (ppm):** δ 9.16 (d, *J* = 1.9 Hz, 2H), 8.67 (s, 2H), 8.54 – 8.48 (m, 4H), 8.30 (d, *J* = 2.0 Hz, 2H), 7.69 (dd, *J* = 8.7, 2.0 Hz, 2H), 1.69 (s, 18H), 1.54 (s, 19H); **MALDI-TOF-MS:** $C_{64}H_{48}D_{12}BN_3$ **Calculated:** 894.088; **Found:** 894.014.

2. Supplementary Figures and Tables

Structural Characterization of Two Emitters.

The synthesis of two emitters emitter is typically achieved by using Suzuki coupling reaction. This method typically involves reactions conducted in a water-toluene mixture, which may induce undesirable hydrogen-deuterium exchange in deuterated precursors, resulting in reduced deuteration ratios. By label each peaks in ^{1}H NMR spectra to corresponding protons of two emitters (Figure S3), we clearly found no signal of the hydrogen resonance from phenylcarbazole was detected in the ^{1}H NMR spectrum of BN-pCzPhD, which means no hydrogen-deuterium exchange in deuterated precursors.

In order to verify the reproducibility and reliability of the observed M/Z, we retested the MALDI-TOF-MS of BN-pCzPhD, the signal at about 894.014 corresponded to BN-pCzPhD, which approximated with the calculated M/Z (894.088). we performed MALDI-TOF-MS of BN-pCzPhD repeatedly, the signals were 893.906 and 893.935, respectively, which all approached with the calculated M/Z. In addition, we also performed MALDI-TOF-MS of BN-pCzPh repeatedly, the signals at about 881.808, 881.814 and 881.921 corresponded to BN-pCzPh, which approximated with the calculated M/Z (882.015). The results have been summarized in the Table S1 and Figure S6. Through these tests, the observed M/Z exhibit a similar deviation from the calculated M/Z, indicating that the discrepancy arises from instrumental measurement.

The single crystals of BN-pCzPh and BN-pCzPhD compounds were successfully obtained via vacuum sublimation method. However, no diffraction signal was observed in single-crystal X-ray diffraction analysis due to the poor quality and defects of the crystals. Moreover, no crystals were obtained via the solvent evaporation method, because of the poor solubility of the two compounds. We further used powder X-ray diffractometer measurement to investigate the powder of BN-pCzPh and BN-pCzPhD crystals. As shown in Figure S7a and S7c, strong and

narrow diffraction peaks appeared in the XRD patterns of BN-pCzPh and BN-pCzPhD. It is inferred that BN-pCzPh and BN-pCzPhD was in a well crystalline state. Furthermore, since deuterium can't be detected by XRD, the diffraction peaks of the two materials exhibit similar characteristics, indicating that they are isotopic isomers with identical structures.

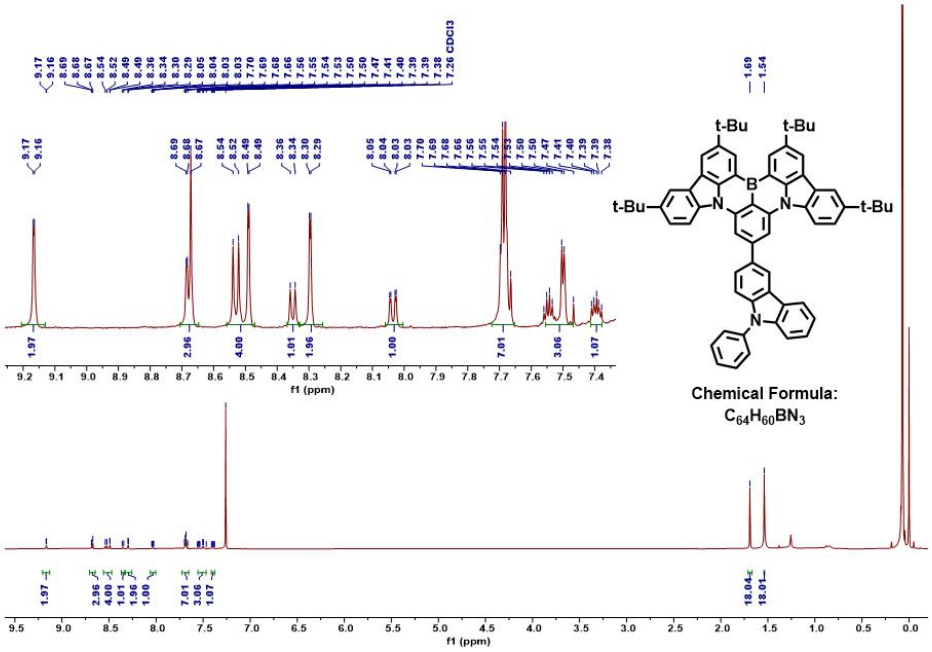

Figure S1. ^{1}H NMR spectrum ($CDCl_3$, 500 MHz) of **BN-pCzPh**.

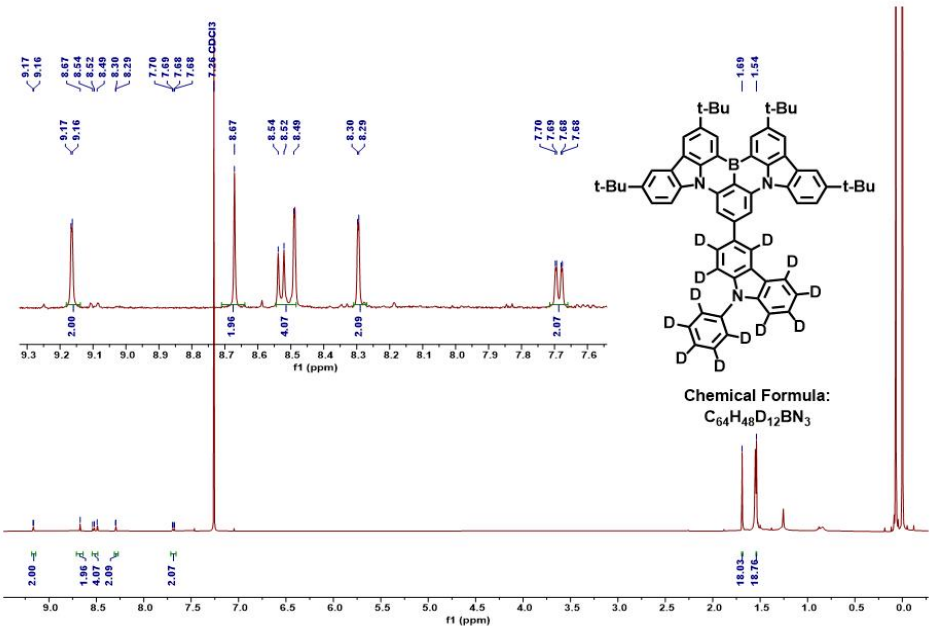

Figure S2. ^{1}H NMR spectrum ($CDCl_3$, 500 MHz) of **BN-pCzPhD**.

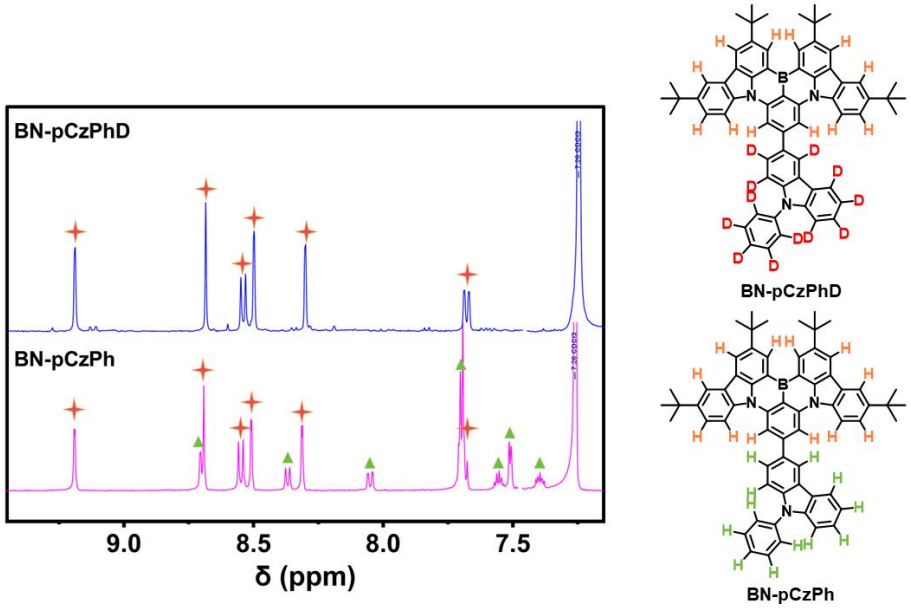

Figure S3. The ^{1}H NMR spectra of **BN-pCzPh** and **BN-pCzPhD** (The orange stars represent the hydrogen on the MR skeleton, the green triangles represent the hydrogen on the phenylcarbazole).

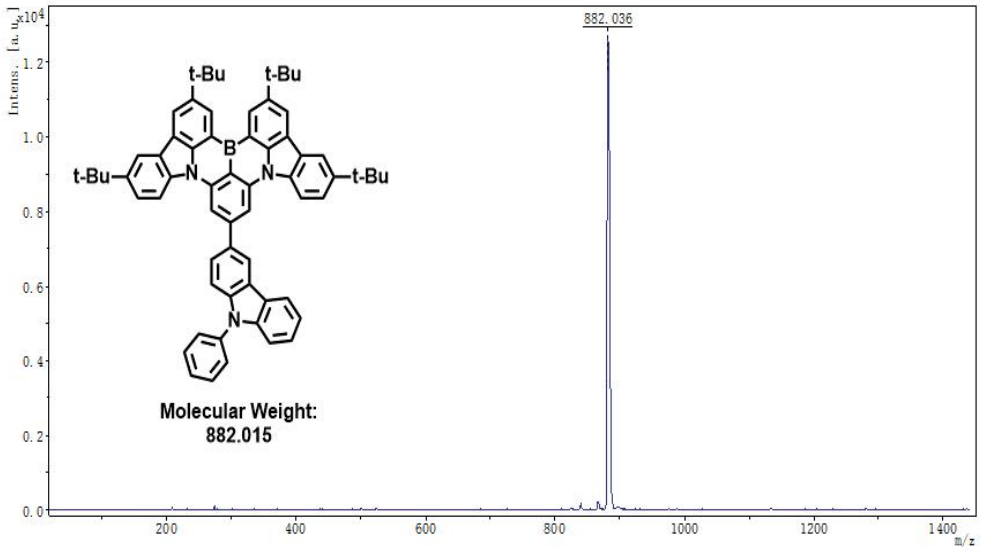

Figure S4. MALDI-TOF-MS of **BN-pCzPh**.

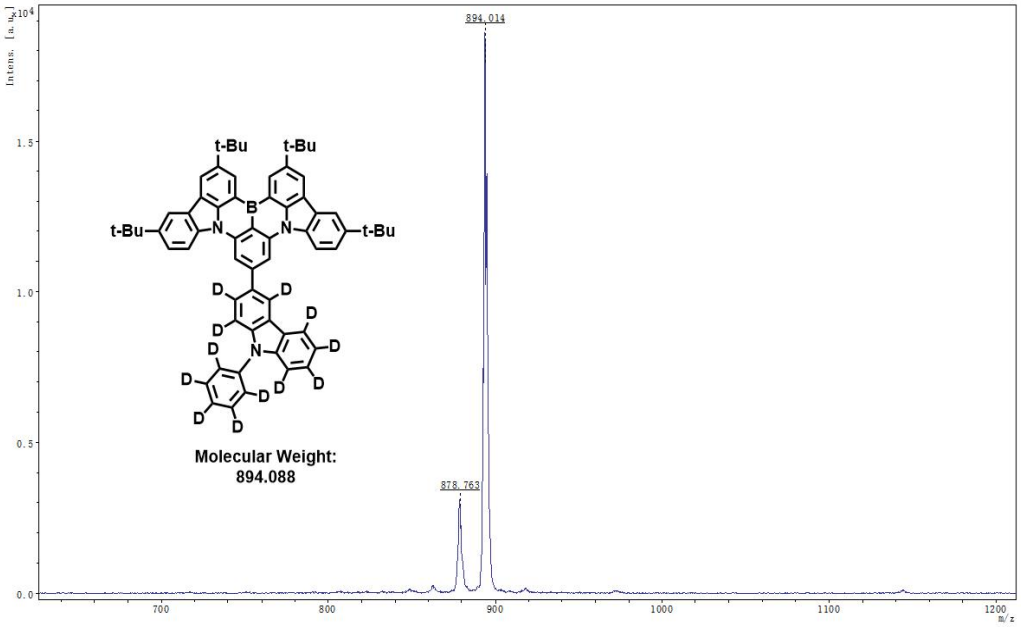

Figure S5. MALDI-TOF-MS of **BN-pCzPhD**.

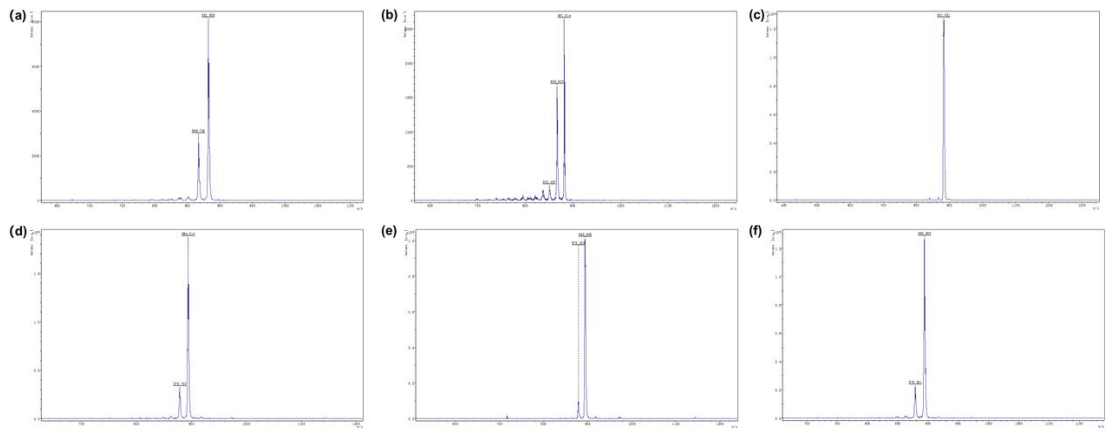

Figure S6. MALDI-TOF-MS of (a) to (c) **BN-pCzPh**; (d) to (e) **BN-pCzPhD**.

Table S1. Summary of the MALDI-TOF-MS for **BN-pCzPh** and **BN-pCzPhD**

Emitter	**BN-pCzPh**	**BN-pCzPhD**
1	881.808	894.014
2	881.814	893.906
3	881.921	893.935

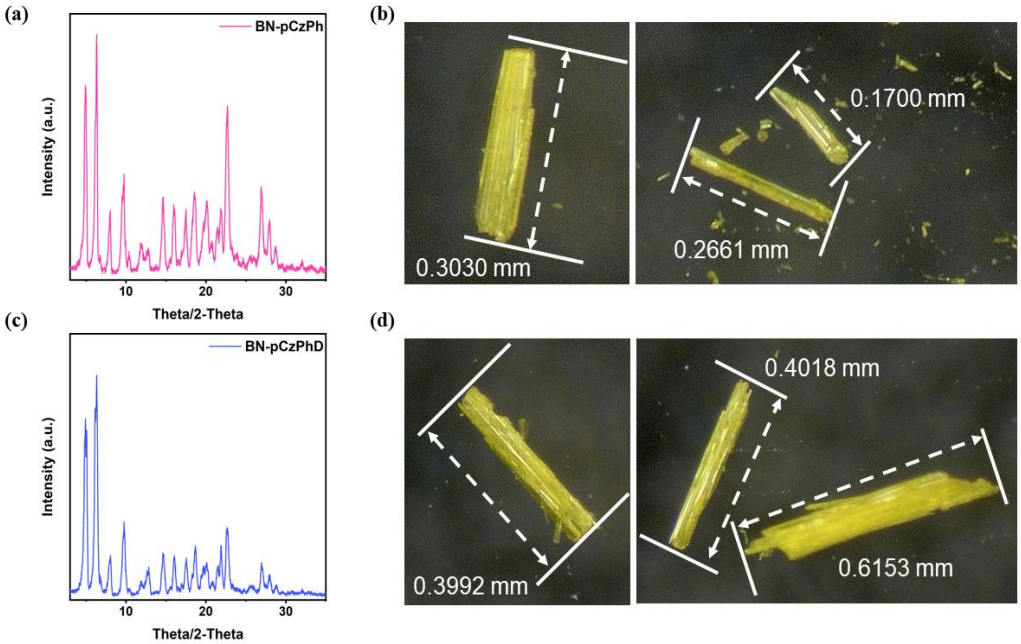

Figure S7. (a) The powder XRD patterns of **BN-pCzPh** crystals; (b) The Single-Crystal image of **BN-pCzPh**; (c) The powder XRD patterns of **BN-pCzPhD** crystals; (d) The Single-Crystal image of **BN-pCzPhD**.

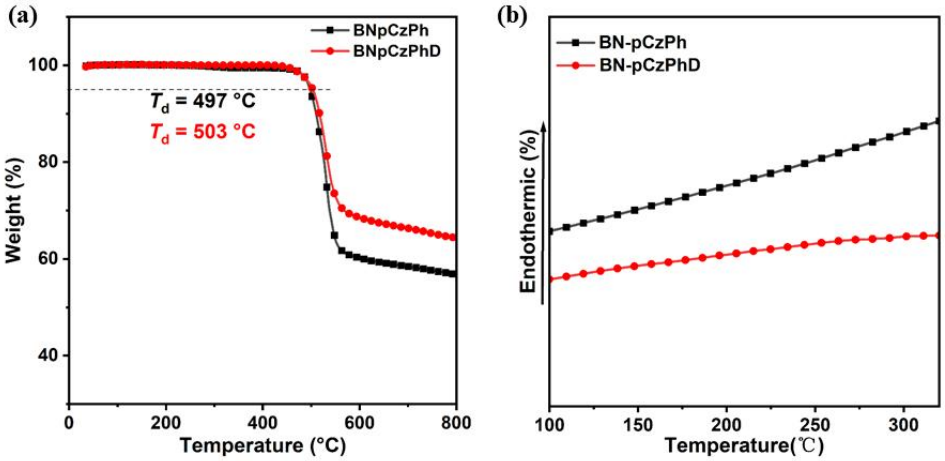

Figure S8. (a) TGA and (b) DSC traces for **BN-pCzPh** and **BN-pCzPhD**

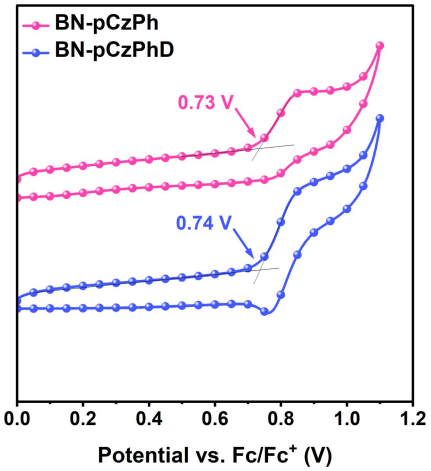

Figure S9. Cyclic voltammograms for **BN-pCzPh** and **BN-pCzPhD** in anhydrous DCM with 0.1 M $TBAPF_6$ as the electrolyte for positive scans, respectively, and Fc^+/Fc redox couple as the internal standard.

DFT Calculations of Two Emitters.

To gain insight into the geometries more accurately, we performed the optimized S_0 geometries using the B3LYP and M06-2X functional with 6-31G(d,p) basis set. As depicted in Figure S10, the optimized S_0 geometries observed in M06-2X adopted the twisted configurations with the dihedral angles of 36.87° between the BCzBN plane and the deuteration donor moiety, which are similar with the molecular geometries observed in B3LYP/6-31G(d,p) level of 40.02°. However, compared with B3LYP

functional, the HOMO and LUMO energies calculated with the M06-2X functional of -4.95 and -1.52 eV, which showed a larger deviation from the result estimated by cyclic voltammetry (CV) of -5.31 and -2.79 eV. The M06-2X functional largely depends on the basis set effect, so the values predicted by M06-2X were not ideal and overestimated in comparison with experimental measurements. In contrast, the B3LYP functional performs better in MR-TADF systems where there is a much larger overlap between hole and electron densities. Owing to the minimal deviation between B3LYP functional calculation results and actual measured values, we chose this functional in DFT calculate.

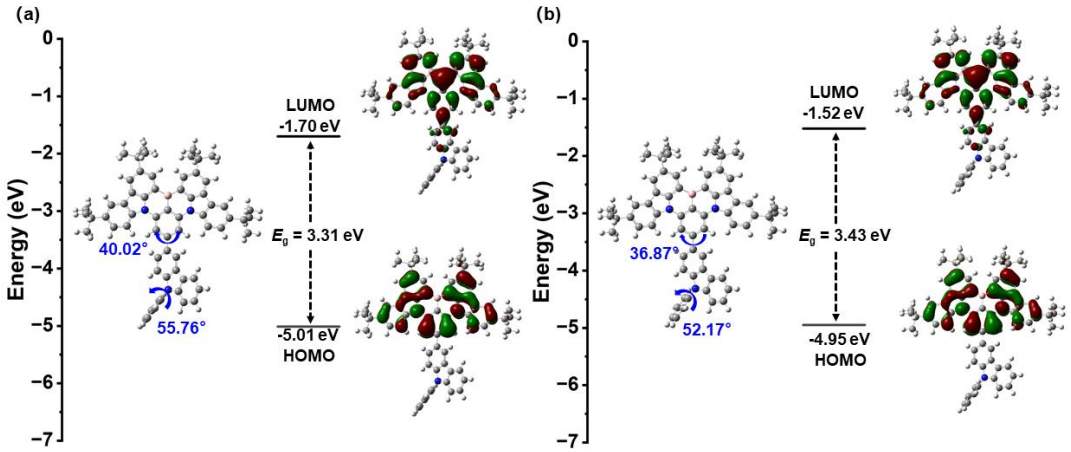

Figure S10. HOMO and LUMO electron density distribution and orbital energies of **BN-pCzPh** calculated at (a) B3LYP /6-31G(d,p) and (b) M06-2X /6-31G(d,p) level in the gas phase.

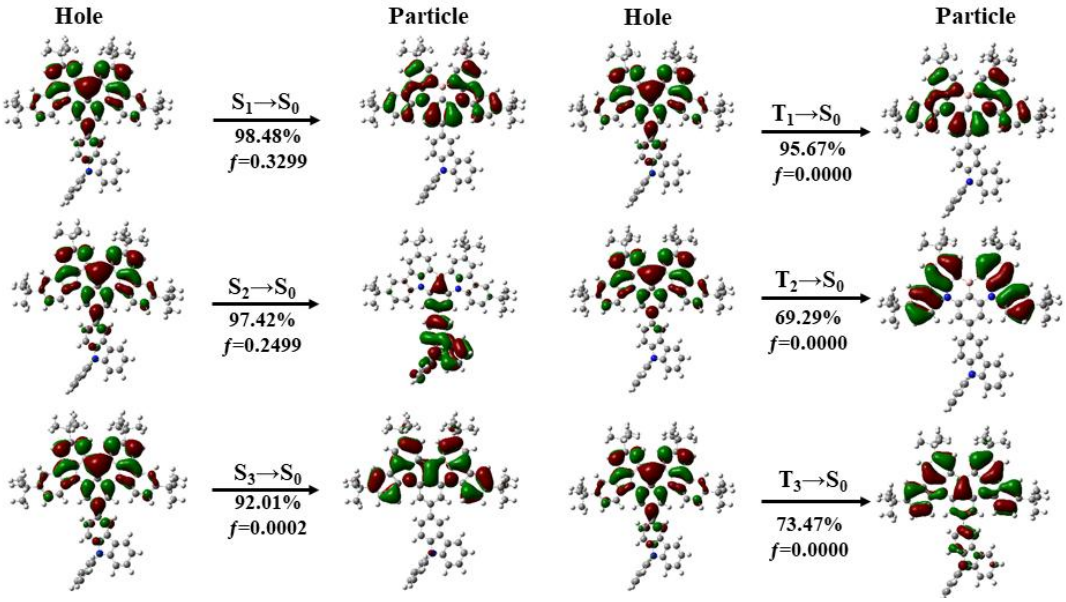

Figure S11. The natural transition orbital distributions of **BN-pCzPh(D)**

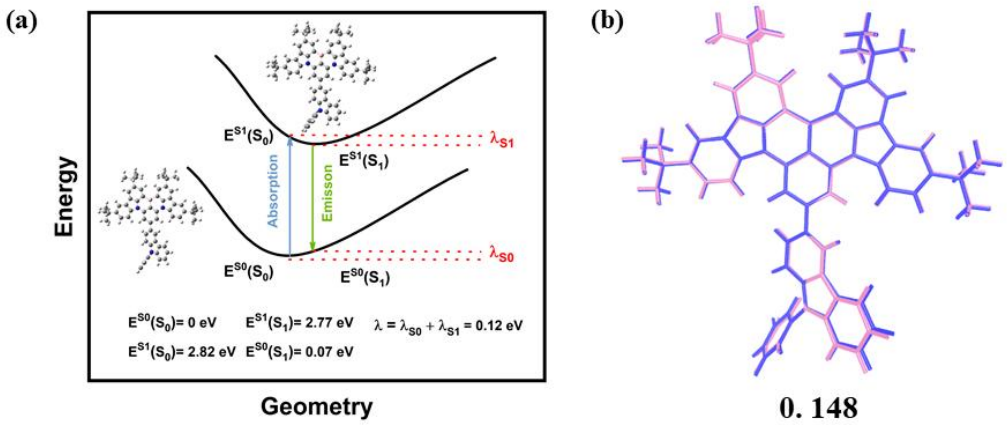

Figure S12. (a) Optimized S_0 and S_1 structures and reorganization energies of **BN-pCzPh(D)** at the B3LYP/6-31G(d,p) level and (b) comparison of the optimized structures of **BN-pCzPh(D)** in S_0 (blue) and S_1 (pink) states.

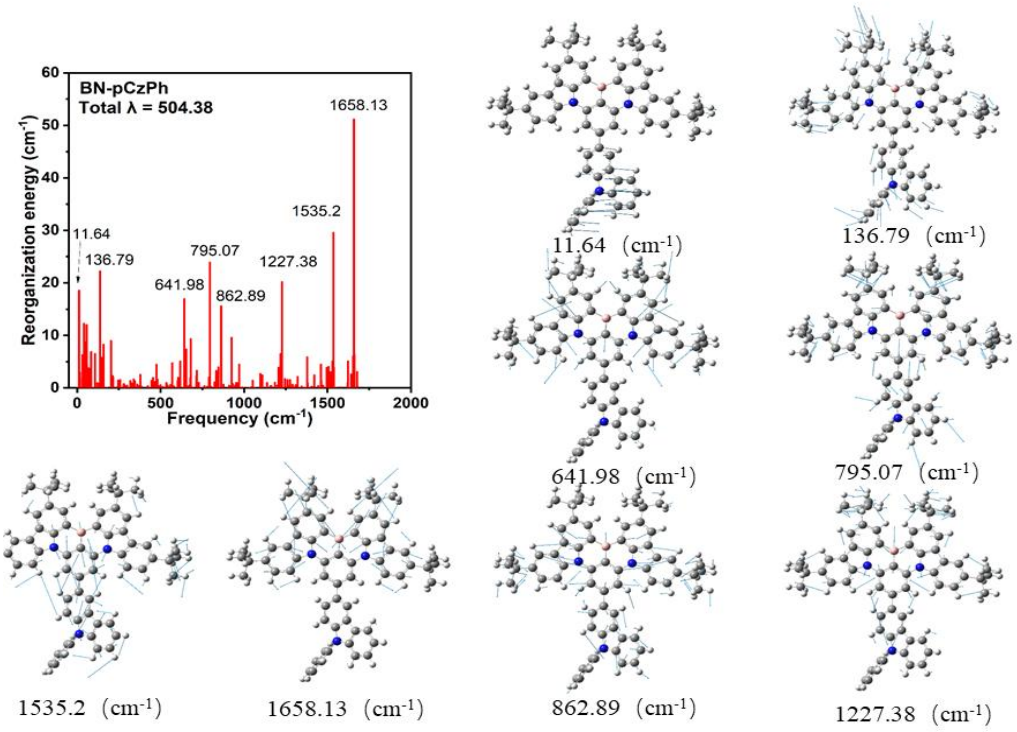

Figure S13. Illustration of selected normal modes contributing to large reorganization energy for the S_0 state of **BN-pCzPh**.

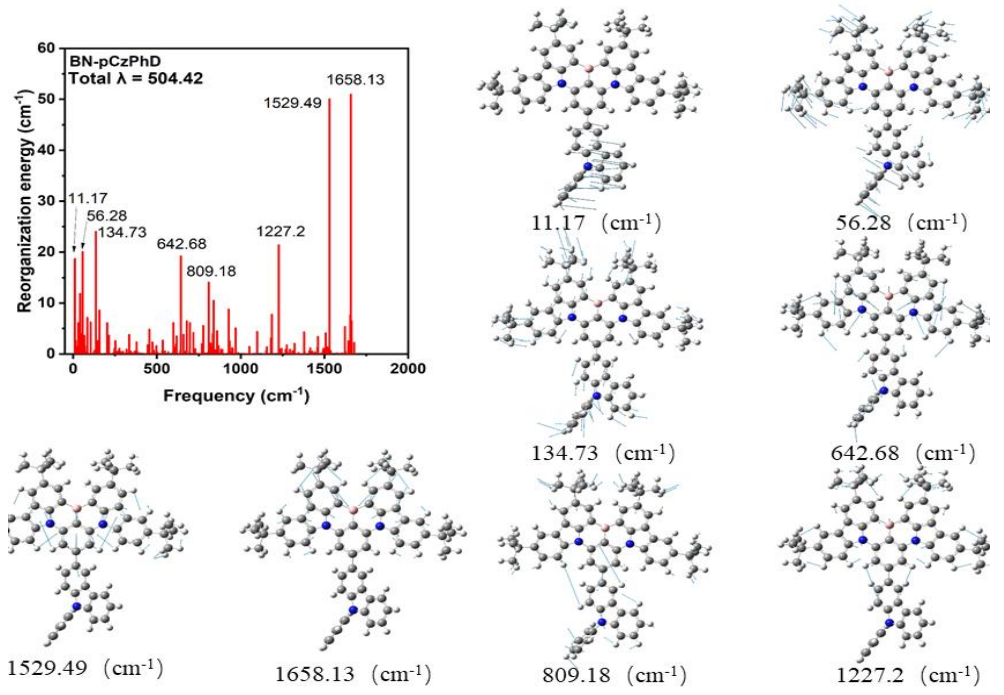

Figure S14. Illustration of selected normal modes contributing to large reorganization energy for the S_0 state of **BN-pCzPhD**.

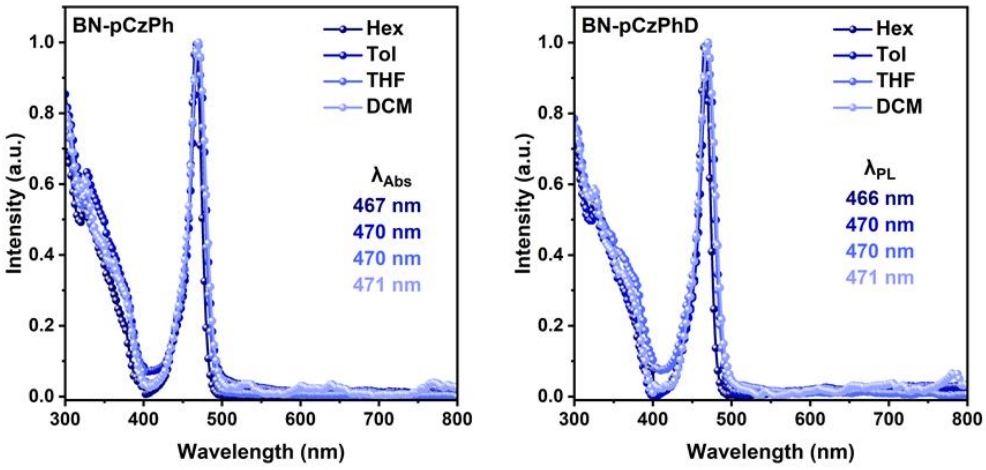

Figure S15. The absorption spectra of **BN-pCzPh** and **BN-pCzPhD** in different polarity solvents (10^{-5} M).

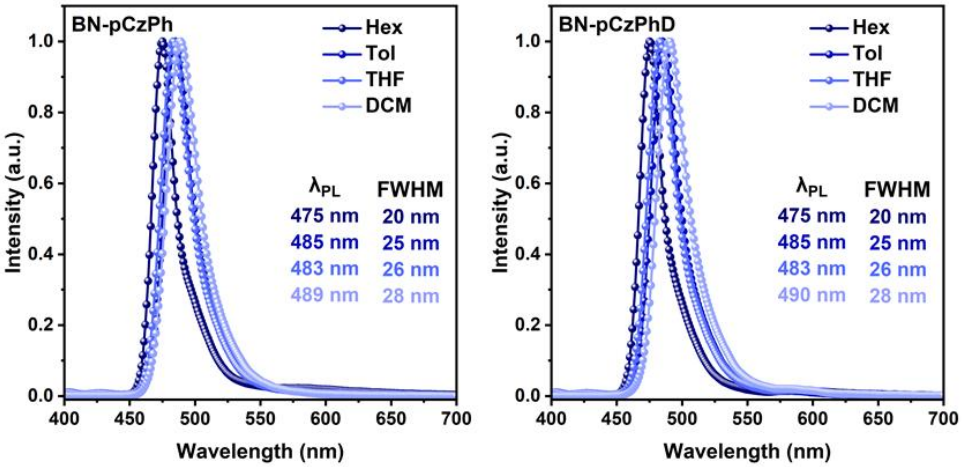

Figure S16. The SS PL spectra of **BN-pCzPh** and **BN-pCzPhD** in different polarity solvents (10^{-5} M, λ_{exc} = 360 nm).

Table S2. Summary of the photophysical properties of **BN-pCzPh** and **BN-pCzPhD**.

Emitters	λ_{abs}[a]	λ_{em}[b]	FWHM[b]	Stokes shift[a]	S_1[a]	T_1[a]	ΔE_{ST}[a]	E_g[a]
	(nm)	(nm)	(nm)	(nm)	(eV)	(eV)	(eV)	(eV)
BN-pCzPh	470	485/493	25 /28	15	2.57	2.49	0.08	2.51
BN-pCzPhD	470	485/492	25/28	15	2.57	2.49	0.08	2.52

[a] Measured in toluene solution with a concentration of 10^{-5} M. [b] Measured in toluene and

doped films (6 wt% doped PhCzBCz films).

Table S3. The absorption and emission bands, FWHM, and Φ_{PL} values of **BN-pCzPh** and **BN-pCzPhD** in solvents of different polarities (10^{-5} M, λ_{exc} = 360 nm).

	BN-pCzPh				**BN-pCzPhD**			
	λ_{abs} (nm)	λ_{PL} (nm)	FWHM (nm)	Φ_{PL} (%)	λ_{abs} (nm)	λ_{PL} (nm)	FWHM (nm)	Φ_{PL} (%)
Hex	467	475	20	90	466	475	20	97
Tol	470	485	25	93	470	485	25	98
THF	470	483	26	92	470	483	26	98
DCM	471	489	28	92	471	490	28	97

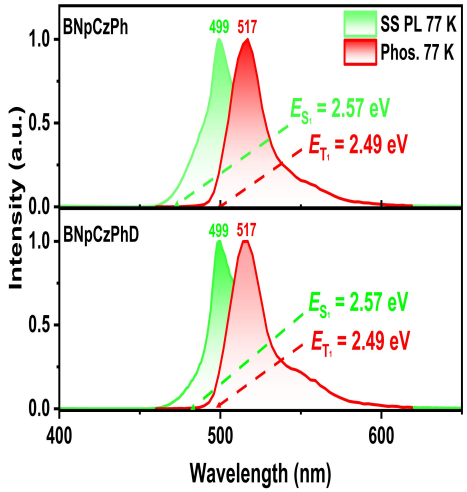

Figure S17. SS PL (77 K) and phosphorescence spectra (1–10 ms, 77 K) of **BN-pCzPh** and **BN-pCzPhD** in toluene (λ_{exc} = 360 nm).

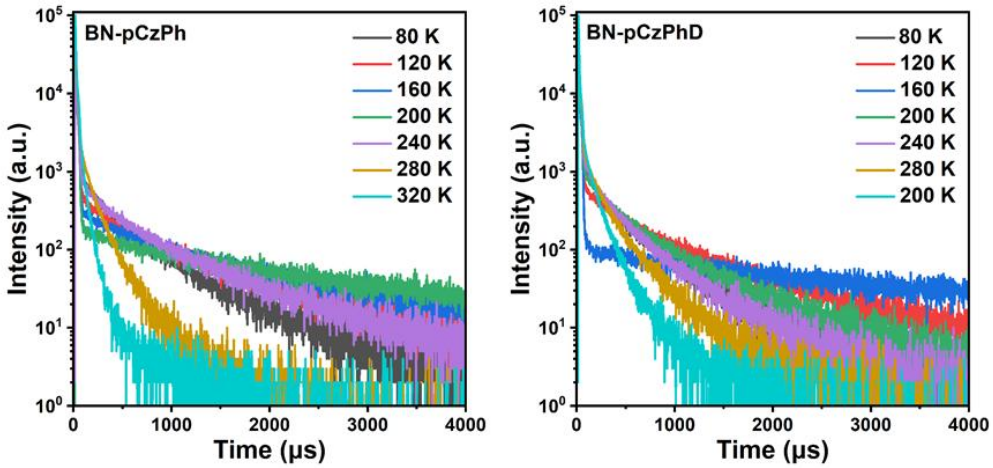

Figure S18. Variable-temperature transient PL decays of 6 wt% doped films of **BN-pCzPh** and **BN-pCzPhD** in host PhCzBCz (λ_{exc} = 360 nm).

Table S4. Detailed photophysical data of 6 wt% doped films of **BN-pCzPh** and **BN-pCzPhD** in host PhCzBCz.

Emitters	Φ_{PL}[a] (%)	Φ_p[b] (%)	Φ_d[c] (%)	τ_p[d] (ns)	τ_d[e] (μs)	k_r[f] (10^8 s^{-1})	k_{nr}[g] (10^6 s^{-1})	k_{ISC}[h] (10^7 s^{-1})	k_{RISC} (10^4 s^{-1})
BN-pCzPh	93	46	47	5.5	42.5	0.83	6.3	9.2	4.8
BN-pCzPhD	98	43	55	5.7	43.8	0.75	1.5	9.8	5.2

[a] The total fluorescence quantum yield. [b] The prompt fluorescent (Φ_F) component of Φ_{PL}. [c] The delayed fluorescent (Φ_{TADF}) component of Φ_{PL}. [d] The lifetimes of prompt fluorescent (τ_F). [e] The lifetimes of TADF (τ_d). [f] The rate constants of radiative decay (k_r). [g] The rate constants of nonradiative decay (k_{nr}). [h] The rate constants of intersystem crossing (k_{ISC}). Φ_p and Φ_d are distinguished from the total Φ_{PL} by comparing the integrated intensities of prompt and delayed components in the transient PL spectra (λ_{exc} = 360 nm).

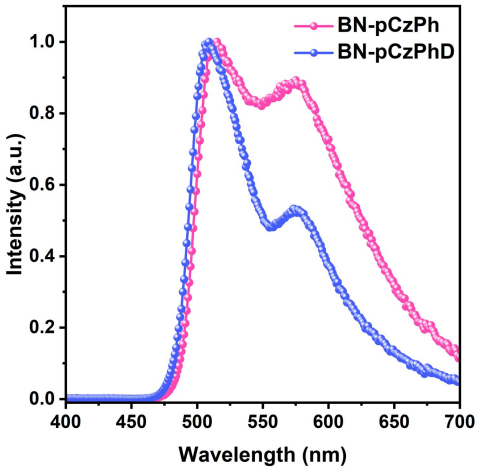

Figure S19. Fluorescence spectra of **BN-pCzPh** and **BN-pCzPhD** in non-doped films (λ_{exc} = 360 nm).

Table S5. The absorption and emission bands, FWHM, and Φ_{PL} values of **BN-pCzPh** and **BN-pCzPhD** in non-doped film (λ_{exc} = 360 nm).

Emitters	λ_{PL} (nm)	FWHM (nm)	Φ_{PL} (%)
BN-pCzPh	515, 575	126	17
BN-pCzPhD	509, 573	90	19

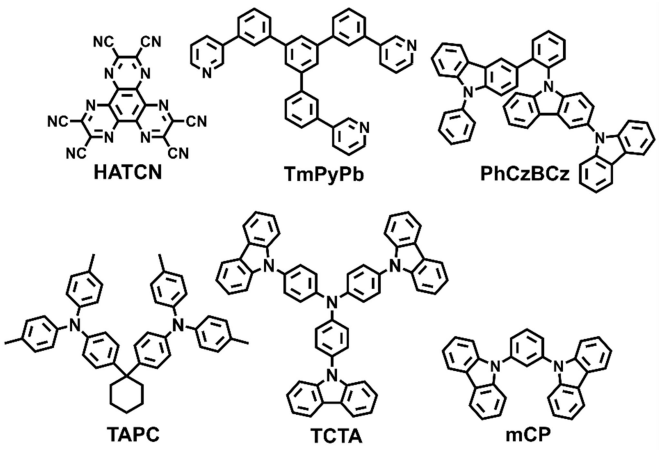

Figure S20. The chemical structures of all transport layers and host material in the doped devices.

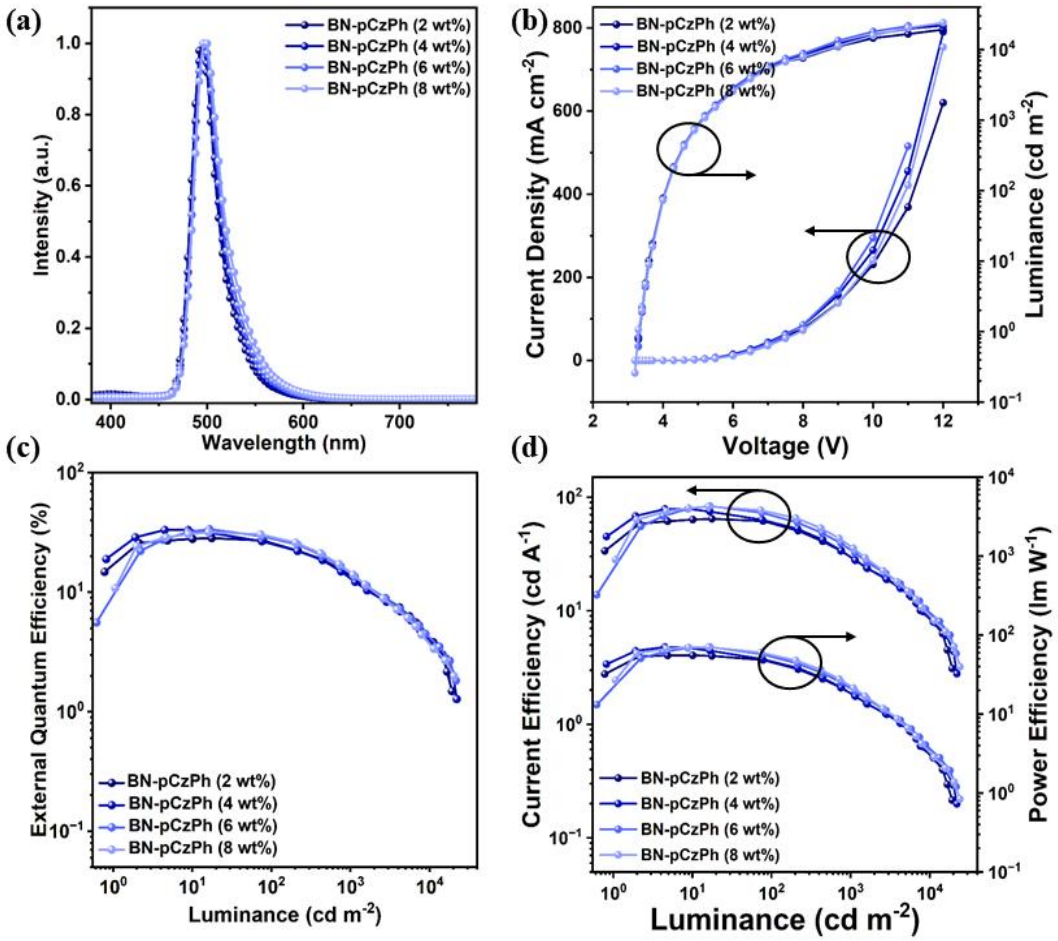

Figure S21. (a) The EL spectra; (b) Luminescence and current density versus voltage; (c) EQE versus luminance curves; (d) CE/PE versus luminance curves characteristics of **BN-pCzPh**-based doped devices at different doping concentrations。

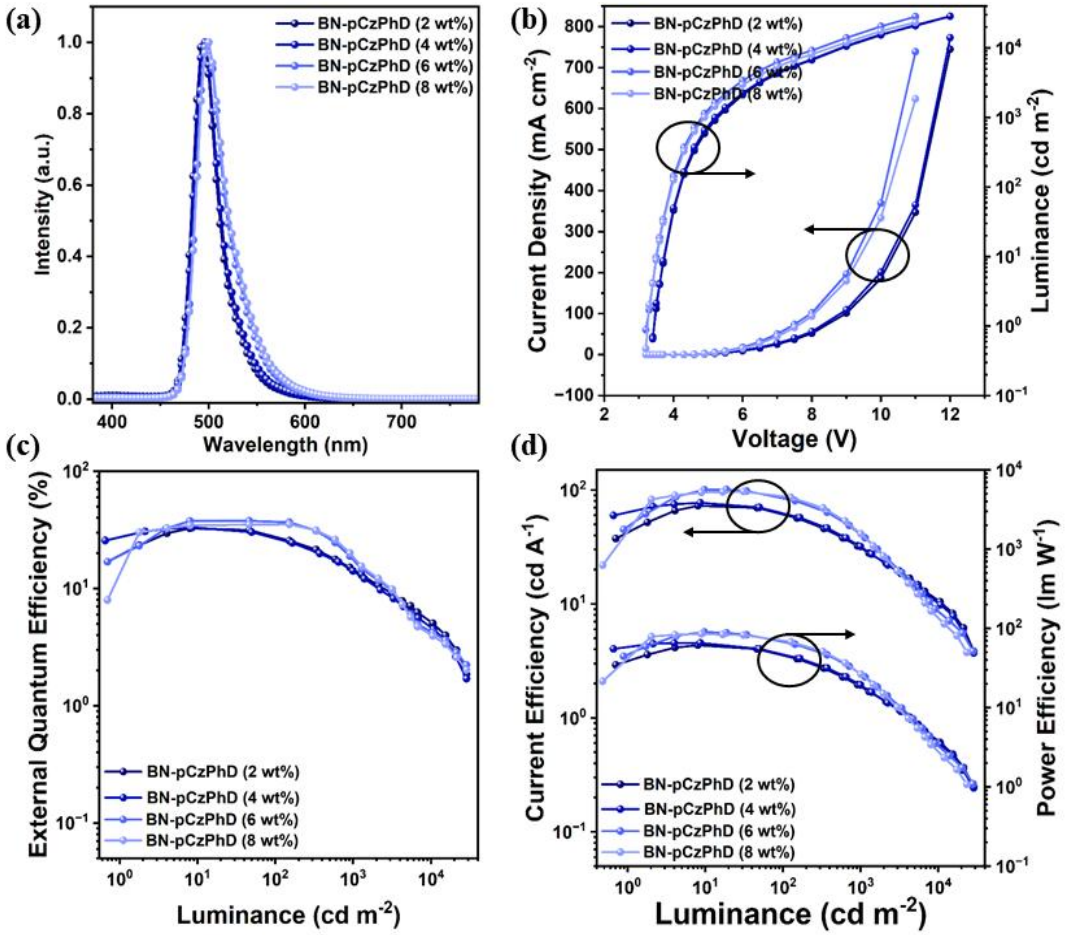

Figure S22. (a) The EL spectra; (b) Luminescence and current density versus voltage; (c) EQE versus luminance curves; (d) CE/PE versus luminance curves characteristics of **BN-pCzPhD**-based doped devices at different doping concentrations.

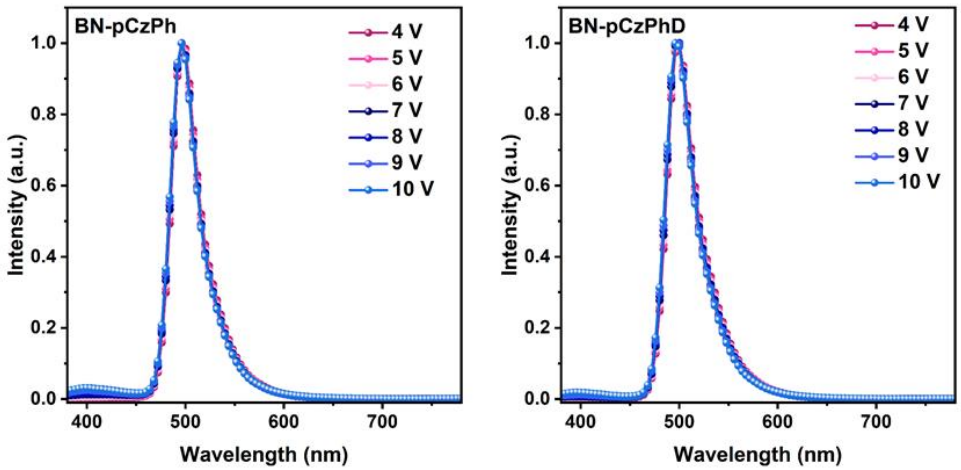

Figure S23. The EL spectra of the best devices (6 wt%) based on **BN-pCzPh** and **BN-pCzPhD** operated at different voltages.

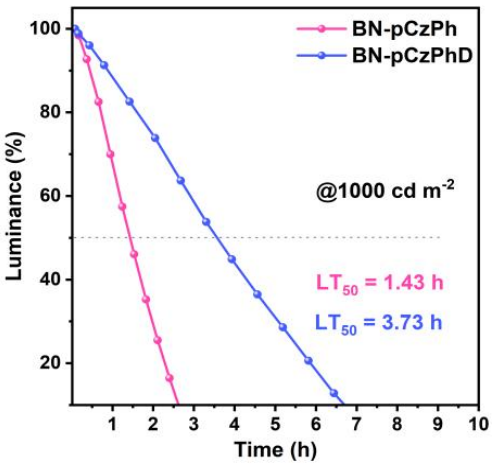

Figure S24. Lifetime measurements of **BN-pCzPh** and **BN-pCzPhD**-based devices with constant current density driving and specified initial luminance (L_0 = 1000 cd m^{-2}).

Table S6. Summary of the EL data for the **BN-pCzPh** and **BN-pCzPhD**-based doped devices at different doping concentrations.

Emitter	Dopant conc. (wt%)	V_{on} [a] (V)	L_{max} [b] (cd m^{-2})	CE_{max} [c] (cd A^{-1})	PE_{max} [d] (lm W^{-1})	EQE [e] (%)	λ_{EL} [g] (nm)	FWHM [h] (nm)	CIE [i] (x, y)
BN-pCzPh	2	3.3	19256	64.4	54.7	28.3/26.3/13.0	496	30	(0.11, 0.49)
	4	3.3	22083	79.0	69.0	33.2/25.8/13.5	496	31	(0.12, 0.51)
	6	3.3	21629	83.7	71.0	33.6/28.5/13.5	496	32	(0.12, 0.53)
	8	3.2	24169	83.2	70.6	31.8/29.5/14.0	496	34	(0.14, 0.56)
BN-pCzPhD	2	3.4	28669	72.7	61.7	32.6/28.5/14.7	496	29	(0.11, 0.49)
	4	3.4	28719	77.5	65.8	33.2/27.7/14.1	496	30	(0.11, 0.51)
	6	3.2	28339	100.9	90.5	37.6/33.2/14.7	500	34	(0.14, 0.57)
	8	3.2	23480	97.1	82.4	35.2/32.4/15.4	500	36	(0.15, 0.58)

[a] Turn-on voltage at the luminescence of 1 cd m^{-2}. [b] Maximum luminance. [c] Maximum current efficiency. [d] Maximum power efficiency. [e] External quantum efficiency of maximum/at 100 cd m^{-2}/1000 cd m^{-2}. [f]EQE roll-offs at 100 cd m^{-2}. [g] EL emission peak of EL spectrum at 6 V. [h] The full width half-maxima of EL spectra. [i] Commission International de l'Éclairage (CIE) coordinates at 6 V.

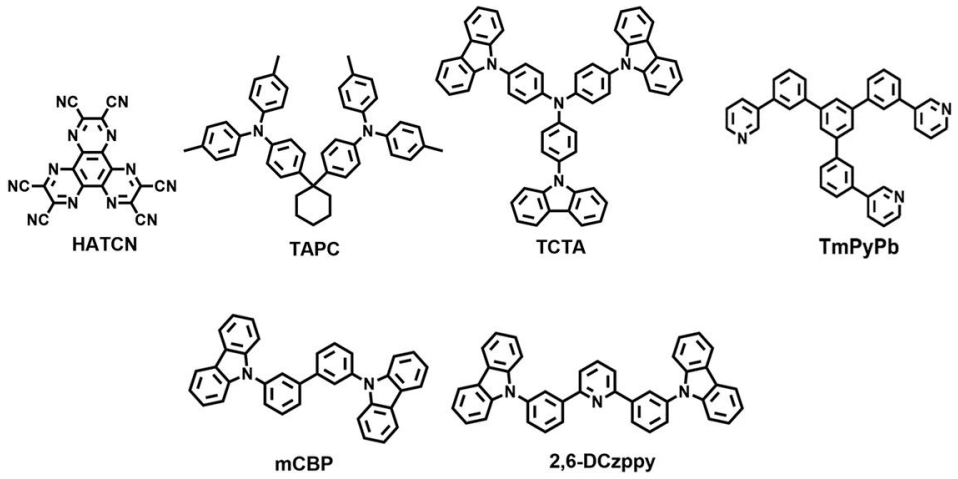

Figure S25. The chemical structures of all transport layers and host material in the doped devices.

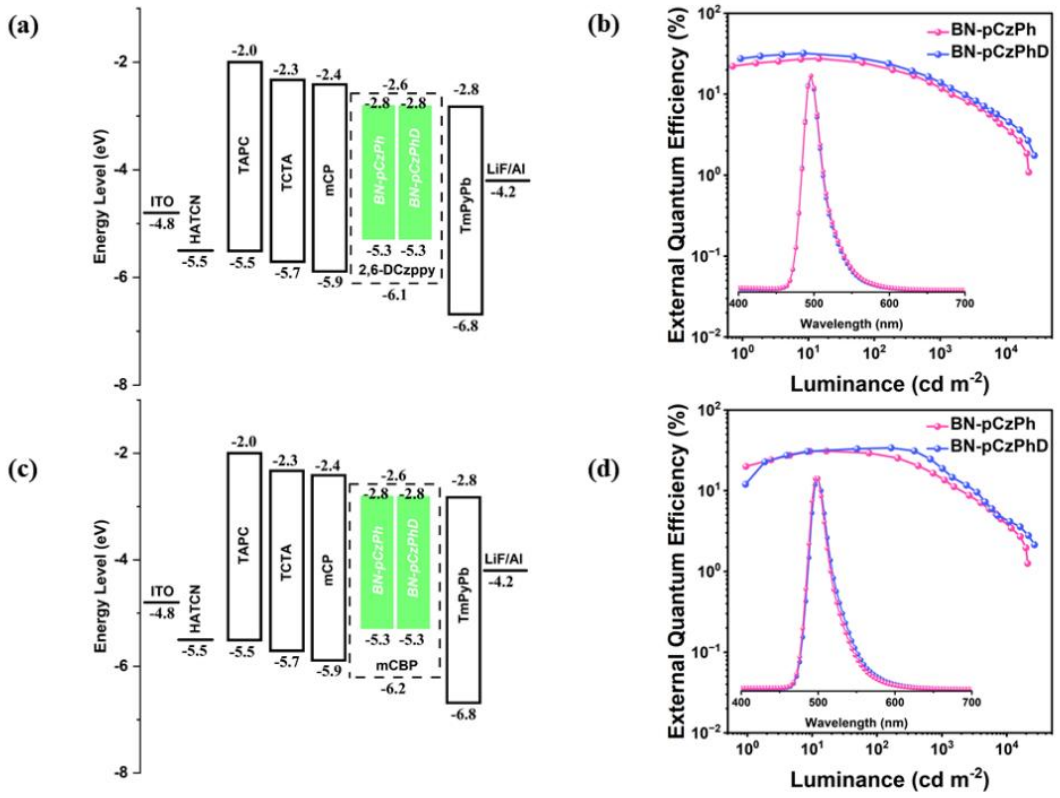

Figure S26. (a) The energy level diagram in the devices and (b) EQE versus luminance curves (inset: the EL spectra) at 6 wt % doping concentration in

2,6-DCzPPy host; (c) The energy level diagram in the devices and (d) EQE versus luminance curves (inset: the EL spectra) at 6 wt % doping concentration in mCBP host.

Table S7. Summary of the EL data for the **BN-pCzPh** and **BN-pCzPhD**-based doped Devices in different host at 6 wt % doping concentrations.

Emitter	host	V_{on}[a] (V)	L_{max}[b] (cd m^{-2})	CE_{max}[c] (cd A^{-1})	PE_{max}[d] (lm W^{-1})	EQE[e] (%)	λ_{EL}[g] (nm)	FWHM[h] (nm)	CIE[i] (x, y)
BN-pCzPh	2,6-DCzPPy	3.3	22074	65.7	55.8	27.6/22.3/11.8	496	31	(0.12, 0.51)
	mCBP	3.3	21004	77.1	65.5	31.0/28.1/13.5	496	34	(0.14, 0.56)
BN-pCzPhD	2,6-DCzPPy	3.4	26890	74.9	63.6	32.1/25.6/13.9	496	32	(0.11, 0.51)
	mCBP	3.2	34317	91.1	77.4	34.0/31.6/14.7	500	36	(0.15, 0.58)

[a] Turn-on voltage at the luminescence of 1 cd m^{-2}. [b] Maximum luminance. [c] Maximum current efficiency. [d] Maximum power efficiency. [e] External quantum efficiency of maximum/at 100 cd m^{-2}/1000 cd m^{-2}. [f]EQE roll-offs at 100 cd m^{-2}. [g] EL emission peak of EL spectrum at 6 V. [h] The full width half-maxima of EL spectra. [i] Commission International de l'Éclairage (CIE) coordinates at 6 V.

Targeted Deuteration Donor Influenced PLQY and Device Performance.

To investigate the influence from the deuteration donor on PLQY, we have evaluated the absolute Φ_{PL} values of BN-pCzPh and BN-pCzPhD in various solvents and doped films. As the polarity of the solvent increased, BN-pCzPhD emitter still displayed high Φ_{PL}s of 97-98% from low-polarity hexane (Hex) to high-polarity dichloromethane (DCM), which significantly higher than that of the BN-pCzPh emitter (90-92%, Table S3). For doped films (6 wt%) using PhCzBCz as the host, the absolute Φ_{PL}s were calculated to be 93% to 98% of BN-pCzPh to BN-pCzPhD (Table S4). To eliminate the influence from the host in doped films, we also prepared non-doped films to evaluate the intrinsic impact of the deuterated donor on Φ_{PL}.

Assigned to the increased degree of π–π stacking (Figure S19), the Φ_{PL} of the two materials are also significantly reduced, from 17% for BN-pCzPh to 19% for BN-pCzPhD (Table S5). However, BN-pCzPhD emitter still displayed higher Φ_{PL} than that of the BN-pCzPh emitter. Owing to the suppression of high-energy vibrations, deuteration remarkably suppresses the non-radiative decay processes of MR-TADF molecules. In fact, BN-pCzPhD exhibited less than a quarter of the k_{nr} values compared with protonated counterparts, contributing to the higher PLQY. These observations suggest that the introduction of deuterated donor units can effectively improve the Φ_{PL} of MR-TADF molecules.

To gain insight into the influence of deuteration donor in device performance, in Figure 4a and S26, the optimized multilayer devices were fabricated with the following structure: ITO/HATCN (5 nm)/TAPC (30 nm)/TCTA (10 nm)/mCP (5 nm)/ 6 wt% emitters in host (30 nm)/TmPyPb (40 nm)/LiF (1 nm)/Al (120 nm) (host = PhCzBCz, mCBP or 2,6-DCzPPy). With the same doping ratio of 6 wt % in three hosts of BN-pCzPh and BN-pCzPhD, the PhCzBCz host exhibited the best device performance with the maximum EQEs of 33.6% and 37.6%, respectively. Obviously, despite employing different hosts, BN-pCzPhD with deuterated donor groups exhibits significantly superior efficiency compared to aprotic material. The maximum EQEs of the BN-pCzPhD-based device in mCBP and 2,6-DCzPPy were 34.0% and 32.1%, respectively, which are higher than that of BN-pCzPh (31.0% and 27.6%, Table S7). The improved EQEs of BN-pCzPhD might be primarily due to its higher PLQY. Due to the suppression of high-energy vibrations that suppresses the non-radiative decay processes, the deuterated donor in the MR-TADF emitter can enhance the intrinsic stability of device. The operational half-lifetimes (LT_{50}) at 1000 cd m^{-2} of BN-pCzPh and BN-pCzPhD-based devices with 6 wt% doping concentration were measured to be 1.43 and 3.73 h. respectively. These results further confirm the positive effect of molecular deuteration on device performance.

3. References

1 Y. Xu, C. Li, Z. Li, J. Wang, J. Xue, Q. Wang, X. Cai, Y. Wang, *CCS Chem.*, 2022, **4**, 2065-2079.

2 X. Dong, S. Shen, Y. Qin, X. Xie, Z. Pang, H. Gao, G. Liu, C.-S. Lee, P. Wang, Y. Wang, *J. Phys. Chem. C.*, 2024, **128**, 974-983.

3 L.Guo, W.Cui, Y.Pu, L.Li, Y.Sun, P.Zheng, C.Li, Y.Wang, *Angew. Chem. Int. Ed*., 2025, **64**, e202518065.

4 Z.Chen, Z.Zhang, Z.Xue, Y.Hu, X.Zhang, J.Miao, C.Pan, C.Yang, *Angew. Chem. Int. Ed.*, 2026, **65**, e23800.

5 T. Hatakeyama, K. Shiren, K. Nakajima, S. Nomura, S. Nakatsuka, K. Kinoshita, J. Ni, Y. Ono, T. Ikuta, *Adv. Mater.*, 2016, **28**, 2777-2781.

6 Y. Kondo, K. Yoshiura, S. Kitera, H. Nishi, S. Oda, H. Gotoh, Y. Sasada, M. Yanai, T. Hatakeyama, *Nat. Photonics*, 2019, **13**, 678-682.

7 Y. Zhang, D. Zhang, J. Wei, Z. Liu, Y. Lu, L. Duan, *Angew. Chem. Int. Ed.*, 2019, **58**, 16912-16917.

8 Y. Zhang, D. Zhang, J. Wei, X. Hong, Y. Lu, D. Hu, G. Li, Z. Liu, Y. Chen, L. Duan, *Angew. Chem. Int. Ed.*, 2020, **59**, 17499-17503.

9 M. Nagata, H. Min, E. Watanabe, H. Fukumoto, Y. Mizuhata, N. Tokitoh, T. Agou, T. Yasuda, *Angew. Chem. Int. Ed.*, 2021, **60**, 20280-20285.

10 Y. Xu, Q. Wang, X. Cai, C. Li, Y. Wang, *Adv. Mater.*, 2021, **33**, 2100652.

11 Y. Zhang, J. Wei, D. Zhang, C. Yin, G. Li, Z. Liu, X. Jia, J. Qiao, L. Duan,

Angew. Chem. Int. Ed., 2022, **61**, e202113206.

12 S. Y. Lee, T. Yasuda, Y. S. Yang, Q. Zhang, C. Adachi, *Angew. Chem. Int. Ed.*, 2014, **53**, 6402-6406.

13 S. Wang, X. Yan, Z. Cheng, H. Zhang, Y. Liu, Y. Wang, *Angew. Chem. Int. Ed.*, 2015, **54**, 13068-13072.

14 Y.-Z. Shi, K. Wang, X. Li, G.-L. Dai, W. Liu, K. Ke, M. Zhang, S.-L. Tao, C.-J. Zheng, X.-M. Ou, X.-H. Zhang, *Angew. Chem. Int. Ed.*, 2018, **57**, 9480-9484.